Optimising proton stopping power ratio prediction with spectral cone-beam CT

Leibold, D.; Schaart, D.R.; Goorden, M.C.

DOI
10.1088/1361-6560/adebd6

Publication date
2025

Document Version
Final published version

Published in
Physics in Medicine and Biology

Physics in Medicine & Biology

Optimising proton stopping power ratio prediction with spectral cone-beam CT

IOP Publishing Phys. Med. Biol. 70 (2025) 145023 https://doi.org/10.1088/1361-6560/adebd6

Physics in Medicine & Biology

IPEM Institute of Physics and Engineering in Medicine

PAPER

Optimising proton stopping power ratio prediction with spectral cone-beam CT

David Leibold[1], Dennis R Schaart[1,2] and Marlies C Goorden[1,*]

[1] Department of Radiation Science and Technology, Delft University of Technology, Mekelweg 15, Delft, The Netherlands
[2] Holland Proton Therapy Center, Huismansingel 4, Delft, The Netherlands
[*] Author to whom any correspondence should be addressed.

E-mail: m.c.goorden@tudelft.nl

Keywords: spectral cone-beam CT, dual-energy CBCT, proton therapy, stopping power ratio, SPR, Cramér–Rao Lower Bound

Supplementary material for this article is available online

OPEN ACCESS

RECEIVED
3 March 2025

REVISED
28 May 2025

ACCEPTED FOR PUBLICATION
3 July 2025

PUBLISHED
16 July 2025

Abstract

Objective. Cone-beam computed tomography (CBCT) is used for patient positioning in proton therapy, but not directly for treatment planning due to its inferior image quality compared to fan-beam CT. One way to improve its value for proton radiotherapy might be to use CBCT setups capable of extracting spectral information, which can be realised through several hardware configurations. Here, we compare different setups w.r.t. to their capability of predicting proton stopping power ratios (SPRs). *Approach*. We investigate six different spectral CBCT realisations in a simulation study, namely a single-source setup with either a dual-layer detector or a photon-counting detector (PCD), a kVp-switching setup with either an energy-integrating detector (EID) or a PCD, and a dual-source setup with either EIDs or PCDs. Our figure of merit is the normalised Cramér–Rao Lower Bound (nCRLB) on SPR variance based on projection data. We take (cross)scatter into account, and compare ideal and realistic detector models to help guide future detector developments. Each setup is optimised w.r.t. source spectra, mAs ratios and energy bin settings (where applicable). *Main results*. Assuming a realistic detector response, setups with a kVp-switching source perform best, with the setup paired with an EID slightly outperforming the PCD-based setup (nCRLBs of 2.74 and 2.81, respectively). However, if the mAs ratio of the kVp-switching source is fixed, the performance of the kVp-switching setup with an EID is significantly degraded (nCRLB = 9.46) and outperformed by PCD-based setups, with nCRLBs of 3.27, 3.45 and 3.60 for the dual-source setup with two PCDs, the single-source setup and the kVp-switching setup with one PCD, respectively. Spectra with higher source voltage or wider spectral separation generally yield lower CRLB values, and avoiding the spectral distortion caused by charge sharing in direct-conversion PCDs promises to lower CRLB values by about a third. *Significance*. We present an extensive comparison of spectral CBCT setups for their application in proton radiotherapy, using a methodology that allows to compare their theoretical limit of performance without being influenced by the choice of reconstruction algorithm or the conversion scheme from Hounsfield units to SPR values.

1. Introduction

Proton radiotherapy is an alternative to conventional photon radiotherapy (Chen *et al* 2023), offering potentially better tissue sparing due to the finite range of protons and since a significant portion of the dose is deposited in the small volume of the Bragg peak (Newhauser and Zhang 2015). However, the same characteristics make the deposited dose distribution susceptible to small changes in the patient's anatomy. An accurate knowledge of the proton stopping power ratio (SPR) of the patient's tissues is therefore required.

The standard workflow of proton therapy consists of scanning the patient prior to treatment with an x-ray fan-beam CT scanner (Bolsi *et al* 2018) in order to perform anatomical delineation and SPR extraction

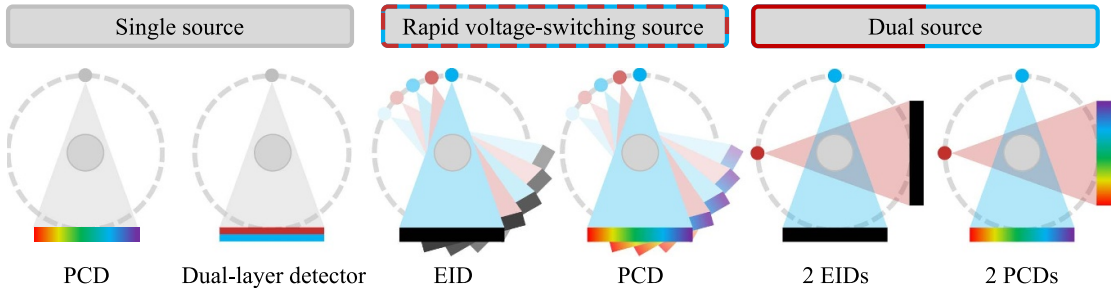

Figure 1. Schematic overview of various possible realisations of spectral (CB)CT that are considered in this work. Adapted with permission from Sandvold *et al* (2024).

on which subsequent treatment planning is based. At the start of each treatment fraction, in-room imaging modalities such as CT-on-rails, flat-panel x-ray radiography or x-ray cone-beam CT (CBCT) are used to position the patient and check the anatomy of the day against the planning CT (Seco and Spadea 2015, Landry and Hua 2018), but not to update the treatment plan directly.

Since proton dose delivery is particularly sensitive to changes in SPR, the adoption of an adaptive treatment workflow in proton therapy is even more warranted than in the case of photon therapy. A more streamlined workflow could potentially make use of the in-room imaging modality (Bolsi *et al* 2018) to update the treatment plan via e.g. image registration (Landry *et al* 2015a, 2015b, Kurz *et al* 2016, Rigaud *et al* 2019, Thummerer *et al* 2020, Huijben *et al* 2024), or ideally even serve directly as the basis for a new treatment plan.

Compared to CT, CBCT offers the advantage of imaging the patient in treatment position, usually without moving the patient table (Landry and Hua 2018). However, the image quality of CBCT is impacted by increased scatter (Siewerdsen *et al* 2005), beam hardening, detector lag (Tanaka *et al* 2010) and patient movement, making it inferior to fan-beam CT. One way of improving CBCT image quality could be to make use of the spectral information contained in the x-ray beam. In case of fan-beam CT, it has been shown that the accuracy and robustness of SPR extraction can be improved by using dual-energy CT (Yang *et al* 2010, Bär *et al* 2017, Taasti *et al* 2017, 2018, Möhler *et al* 2018, Wohlfahrt *et al* 2018, Xie *et al* 2018, Moskvin *et al* 2022, Peters *et al* 2022) compared to classical single-energy CT. It is therefore reasonable to expect that spectral CBCT can also improve SPR extraction compared to single-energy CBCT.

In single-energy CT, a source operating at a fixed voltage is paired with an energy-integrating detector (EID). The term *spectral CT* as used here refers to any CT implementation in which information contained in the x-ray spectrum is utilised for imaging. Spectral CT can be realised by imprinting spectral information on the source, by extracting it using a suitable detector, or by a combination thereof. Possible implementations are (see figure 1):

- A single x-ray source operating at a fixed voltage with a photon-counting detector (PCD),
- A single source operating at a fixed voltage with a dual-layer detector,
- A rapid voltage-switching source with an EID,
- A rapid voltage-switching source with a PCD,
- Two sources at different fixed voltages coupled with an EID each,
- Two sources at different fixed voltages coupled with a PCD each.

These implementations vary in their complexity and cost. Hence, a comparison of their performance on the task of SPR extraction is warranted to guide further technological developments of spectral CBCT for proton therapy, and will be conducted in this simulation study.

A common approach for comparing different setups w.r.t. their performance is to acquire either real or simulated scan data, reconstruct Hounsfield unit (HU) maps at different energies, use a conversion scheme from HU to SPR values—either via calibrating a relationship between measured HU values and SPR (Schneider *et al* 1996, Taasti *et al* 2016, Peters *et al* 2023) or via a more physics-based approach (Yang *et al* 2010, Saito 2012, Li *et al* 2017)—and finally compare the predicted SPR values in image space to the ground truth. However, in case of a discrepancy between ground truth and predicted SPR values, it is not clear whether this is due to limitations in the detection and data acquisition process, the reconstruction algorithm, or the conversion scheme from HU to SPR. We therefore opted for a different approach using the Cramér–Rao Lower Bound (CRLB), which, in simple terms, quantifies the information that is available in the acquired sinograms w.r.t. to the extraction of SPR. The CRLB states the lowest possible variance with

which an unbiased estimator can extract SPR information from the acquired sinograms. The advantage of this approach is that it circumvents limitations of reconstruction algorithms or of HU to SPR conversion schemes, and that it does not require knowledge of an explicit analytical expression for the relationship between the acquired sinogram data and SPR. We employ this CRLB-based approach in a simulation study, since comparing and optimising a large number of different spectral CBCT setups with various parameters is feasible in a simulation but not experimentally. Furthermore, determining the CRLB requires taking derivatives of SPR w.r.t. tissue parameters, a large number of measurement repetitions and an extremely stable source output, which is onerous if not impossible to perform in an experimental setup. In contrast, a study in silico allows to precisely control the acquisition parameters as well as ensure a fair comparison between different spectral CBCT implementations, and it allows to individually probe the influence of various degradation mechanisms on the overall performance.

Our simulation study builds on previously published work in the field, starting with the seminal paper on dual-energy CT by Alvarez and Macovski (1976) who used the CRLB to arrive at expressions for the standard deviation on the estimation of material line integrals. The use of the CRLB as a figure of merit has since been adopted for optimising various aspects of x-ray imaging systems, for example for optimising bow-tie filters (Hsieh and Pelc 2015), the processing of PCD signals (Hsieh and Pelc 2016), charge sharing correction algorithms (Taguchi 2021) or PCD binning (Wang *et al* 2011, Wang and Pelc 2011). Our study is most closely related to the work by Roessl and Herrmann (2009) who investigated the effect of PCD threshold values on material decomposition as well as the optimum layer thicknesses for dual-layer detectors, and to the work by Cai *et al* (2023) who optimised a dual-layer setup with various filtration materials for use as both a single- and dual-energy modality.

The aforementioned literature focuses on setup optimisation for imaging tasks such as material decomposition and K-edge imaging. In this work, we compare and optimise the possible implementations of spectral CBCT listed above for extraction of SPR. Since scatter significantly degrades CBCT image quality, we also include a realistic scatter component obtained from Monte-Carlo (MC) simulations. We first compare highly idealised setups in order to show the theoretical limits of what could be achieved, which might help to guide further developments in detector design by highlighting the areas with the largest potential for performance gains. We then take into account a more realistic detector response in our simulations, which gives an indication of what can be expected based on the currently available detector technology.

2. Methodology

2.1. Overview

The aim is to compare different implementations of spectral CBCT (section 2.2) with respect to their ability to extract SPR. Our figure of merit is the variance on the estimated SPR values, as given by the CRLB (section 2.4), compared at equal dose (section 2.6). The material properties of the object (section 2.5) determine the spectrum of photons arriving at the detector, comprised of a primary component and a scatter component. For computational speed, we calculate the primary component using the Lambert–Beer law, whereas the scatter component is determined via MC simulations (section 2.7). To arrive at the detected signal, both an idealised and a realistic detector response are compared (section 2.8). Figure 2 gives an overview of the workflow of our methodology.

2.2. Spectral CBCT setups

Section 1 and figure 1 list the investigated spectral CBCT setups, which are described in more detail in the following.

Each setup uses one of the following types of detector:

- **PCD:** a PCD outputs the number of events that are registered in each of a given number of energy bins during the exposure time. In case of an ideal detector response, the incoming spectrum is perfectly registered and separated into the desired number of energy bins. In case of a realistic detector response, the detector material is set to cadmium telluride (CdTe; mass fractions: $f_{\mathrm{Cd}} = 0.4684$; $f_{\mathrm{Te}} = 0.5316$; mass density: $\rho_{\mathrm{mass,\ CdTe}} = 5.85\,\mathrm{g\,cm^{-3}}$) of 1.6 mm thickness. See section 2.8 for more information on the modelling of detector responses.
- **EID:** an EID outputs the total deposited energy during the exposure time, that is, the sum over the number of deposited events, each multiplied by their energy. In case of an ideal detector response, the incoming spectrum is fully deposited. In case of a realistic detector response, the detector material is set to caesium iodide (CsI; mass fractions: $f_{\mathrm{Cs}} = 0.5115$; $f_{\mathrm{I}} = 0.4885$; mass density: $\rho_{\mathrm{mass,\ CsI}} = 4.51\,\mathrm{g\,cm^{-3}}$; its scintillation-inducing dopant (e.g. Tl) is neglected) of 1.9 mm thickness (equivalent to 1.6 mm CdTe based on equal deposited energy by an incoming RQA9 spectrum (I E Commission 2005)).

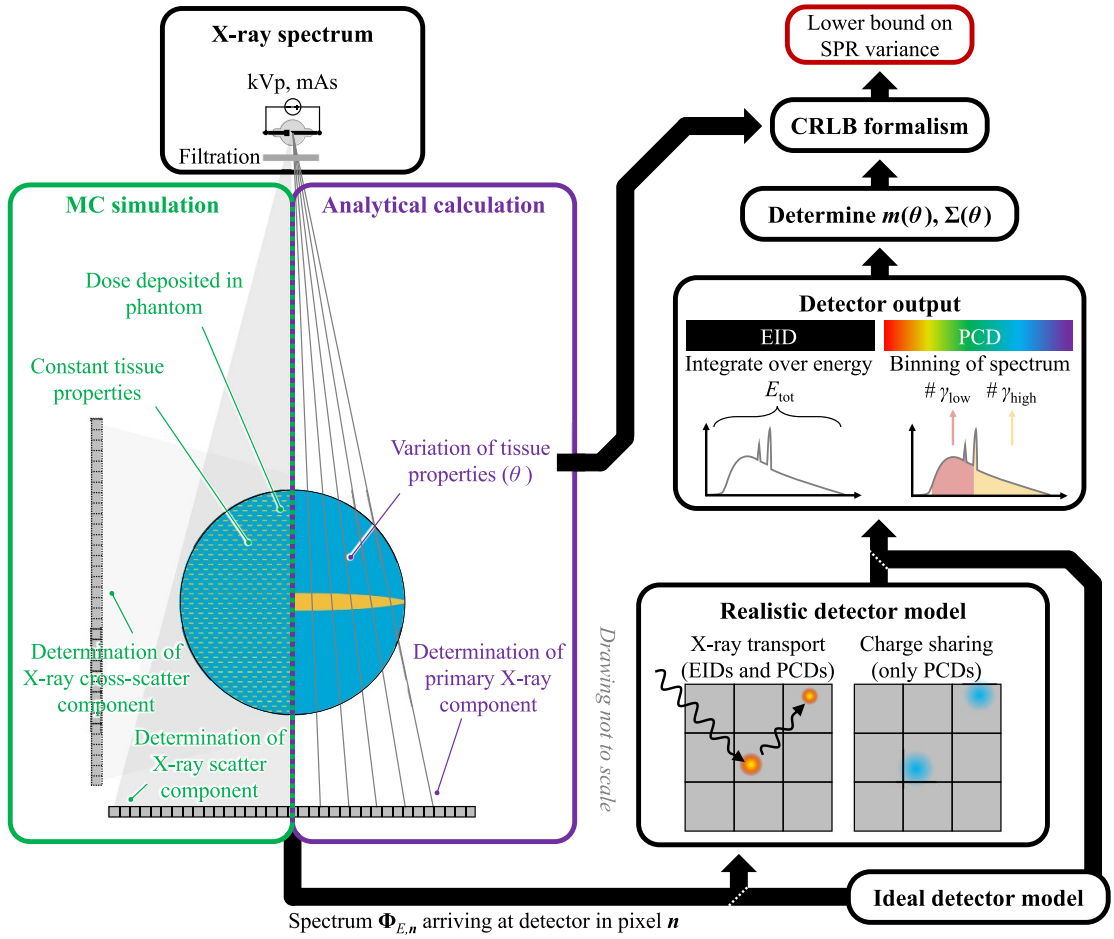

Figure 2. Schematic overview of the workflow of our methodology. For explanations we refer to the following sections: section 2.6: x-ray spectra and deposited dose, section 2.7: x-ray scatter originating in the phantom, section 2.8: detector response function, section 2.4: Cramér–Rao Lower Bound formalism.

- **Dual-layer detector:** the dual-layer detector consists of two detector layers with a filtration layer sandwiched in between them; each detector layer acts as an EID.

  An ideal dual-layer detector is considered to be capable of perfectly separating the spectrum into a low (LE) and high energy (HE) region, and it is modelled based on three energy bins: The lowest and highest energy bin represent the top and bottom layer, respectively, each being read out in the fashion of an EID. The third energy bin, located between the LE and HE bin, acts as an ideal filtration layer; all photons registered in this bin are discarded.

  In case of a realistic detector response we assume that the dual-layer detector consists of two CsI detector layers and, if applicable, a copper filtration layer; other layers such as silicon-based photodetection layers are neglected.

  Please note that 'top layer' refers to the layer of the detector that faces the source.

For the x-ray source we assume ideal behaviour, in that it can supply any desired voltage and any desired product of current and exposure time (commonly referred to as mAs), and in that it can be considered a point source. Furthermore, it is assumed that the x-ray source can switch between any two mAs and/or voltage levels instantaneously. The investigated source voltages range from 80 to 140 kVp in steps of 20 kVp. Optional source filtration based on tin (Sn) with thicknesses between 0.2 to 0.8 mm covers the range used in commercial CT scanners.

In case of dual-source setups, cross-scatter between source-detector pairs is included and filtration can be adjusted individually for each source, unlike in a kVp-switching setup where no cross-scatter is present and filtration affects both the LE and HE phase of the source simultaneously.

Table 1 outlines the parameters that are optimised for each setup. Figure 3 illustrates the optimised parameters using two setups as representative examples; for all other setups, the optimised operating parameters are a subset of the ones shown in figure 3. The optimisation is performed by conducting a grid search exploring all possible combinations of all parameters of a setup, which is feasible since the

Table 1. List of the investigated spectral CBCT setups and respective optimised parameters. LE: low energy; HE: high energy.

Spectral CBCT setup	Optimised parameters
Single-source setup with PCD	• Source voltage • Source filtration for the best performing source voltage • Thresholds of energy bins
Single-source setup with dual-layer detector	• Source voltage • Source filtration for the best performing source voltage • In case of ideal detectors: thresholds of energy bins (including the bin acting as a filtration layer). In case of realistic detectors: thicknesses of top, bottom and filtration layer.
kVp-switching setup with EID	• Combination of source voltages • Source filtration for the best performing source voltage pair (filtration affects both the LE and HE spectra simultaneously) • Ratio mAs_{LE} : mAs_{HE}
Dual-source setup with EIDs	• Combination of source voltages • Source filtration for the best performing source voltage pairs (filtration for each source is independent) • Ratio mAs_{LE} : mAs_{HE}
kVp-switching setup with PCD	• Combination of source voltages • Source filtration for the best performing source voltage pair (filtration affects both the LE and HE spectra simultaneously) • Ratio mAs_{LE} : mAs_{HE} • Thresholds of energy bins
Dual-source setup with PCDs	• Combination of source voltages • Source filtration for the best performing source voltage pair (filtration for each source is independent) • Ratio mAs_{LE} : mAs_{HE} • Thresholds of energy bins

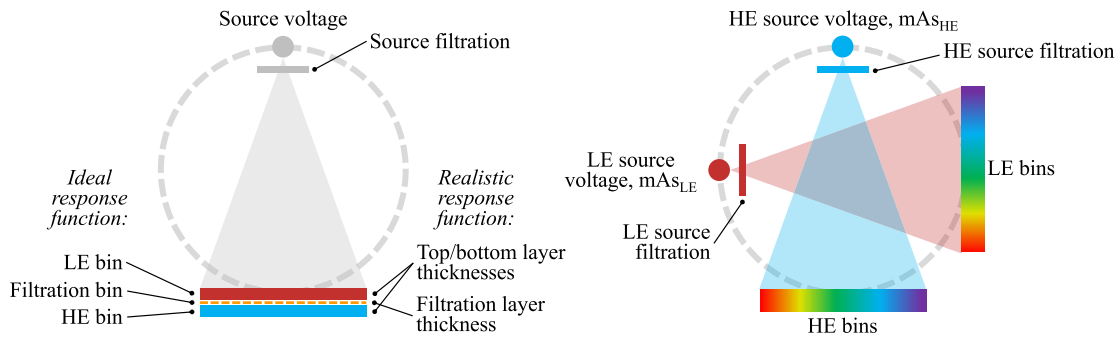

Figure 3. Representative examples of optimised parameters in case of a single source combined with a dual-layer detector (left) and a dual-source setup combined with two PCDs (right). The optimised parameters for the dual-layer detector differ between the case of assuming an ideal or realistic detector response function (see explanations in the text). The optimised operating parameters for all other setups are a subset of the parameters shown here. LE: low energy; HE: high energy. Adapted with permission from Sandvold *et al* (2024).

computation time of our CRLB implementation takes a few seconds per parameter and detector pixel. The only exception is the parameter of source filtration, which is only optimised for the best performing source voltage (pair). In the following, a more detailed account is given:

- **Single source operating at a constant voltage and single PCD:** we compare PCDs with two, three and four energy bins, corresponding to three, four and five thresholds with the bottom threshold of the lowest energy bin always fixed at 20 keV, and the upper threshold of the highest energy bin fixed at the energy corresponding to the source voltage (this also applies to all other setups using PCDs with a similar configuration). The

positions of all non-fixed thresholds are optimised using step sizes of 2 (5) keV for the PCDs with two and three (four) energy bins, taking into account all possible combinations of threshold values.

Furthermore, we investigate PCDs with near-continuous binning, using bins with 1 keV width, as a reference, since they should be able to utilise the spectral information to its fullest.

Additional Sn source filtration is investigated for the best performing 140 kVp source spectrum.

- **Single source operating at a constant voltage and dual-layer detector:** when assuming an ideal detector, the bottom threshold of the LE bin is fixed at 20 keV, and the upper threshold of the HE bin is fixed at the energy corresponding to the source voltage. The upper threshold of the LE bin and the bottom threshold of the HE bin are optimised using a step size of 2 keV, taking into account all possible combinations of threshold values, which includes the width of the third interjacent bin representing the filtration layer.

  For a realistic detector, the combined thickness of the top and bottom layer is kept fixed at 1.9 mm CsI. For the top (bottom) layer, thicknesses from 0.05 to 0.8 mm (1.85 to 1.1 mm) are investigated in step sizes of 0.05 mm. The thickness of an additional copper filtration layer is varied from 0.2 to 4.25 mm.

  Additional Sn source filtration is investigated for the best performing 140 kVp source spectrum.
- **Single rapid voltage-switching source and single EID:** we investigate all possible pairs of source voltages between 80 kVp and 140 kVp. For the best performing voltage pair of 80 kVp/140 kVp we investigate additional Sn source filtration.

  The investigated range of $\mathrm{mAs_{LE}} : \mathrm{mAs_{HE}}$, that is, the ratio of the product of source current and exposure time for the LE phase ($\mathrm{mAs_{LE}}$) and for the HE phase ($\mathrm{mAs_{HE}}$) of the source, is set individually for each spectrum combination such that the optimum falls within the covered range, with a lower limit for the ratio of 1 : 2 and an upper limit of 30 : 1.
- **Two sources at different fixed voltages coupled with an EID each:** the optimisation of operating parameters for this setup differs from the previous one only in that the filtration for the low and HE source spectrum are adjusted independently. Additional filtration is investigated for both the 80 kVp/140 kVp and 100 kVp/140 kVp voltage pair. The investigated range of the ratio $\mathrm{mAs_{LE}} : \mathrm{mAs_{HE}}$ is set individually for each spectrum, with a lower limit of 1 : 4 and an upper limit of 60 : 1.
- **Single rapid voltage-switching source and single PCD:** we investigate all possible pairs of source voltages between 80 kVp and 140 kVp. For the best performing voltage pair of 80 kVp/140 kVp we investigate additional Sn source filtration.

  The investigated range of the ratio $\mathrm{mAs_{LE}} : \mathrm{mAs_{HE}}$ ranges from 1 : 100 000 to 10 000 : 1, that is, in between the limits that only the HE or only the LE source is active.

  A PCD with two energy bins is investigated, and its non-fixed threshold is set individually for the duration of the LE and HE phase of the source and optimised using a step size of 5 keV, taking into account all possible combinations of LE and HE bin threshold values.
- **Two sources at different fixed voltages coupled with a PCD each:** the optimisation of operating parameters for this setup differs from the previous one only in that the filtration for the low and HE source spectrum is adjusted independently. As before, PCDs with two energy bins are assumed, and their thresholds are optimised independently using a step size of 5 keV.

2.3. Calculation of SPRs

According to the Bethe equation (Ödén *et al* 2015) the SPR, that is, the proton stopping power of a material relative to water, can be calculated as

$$\mathrm{SPR} = \frac{\rho_{\mathrm{elec,\,mat}}}{\rho_{\mathrm{elec,\,water}}} \cdot \frac{\ln\left(\frac{2m_e c^2\beta^2}{I_{\mathrm{mat}}\cdot(1-\beta^2)}\right) - \beta^2}{\ln\left(\frac{2m_e c^2\beta^2}{I_{\mathrm{water}}\cdot(1-\beta^2)}\right) - \beta^2}\quad , \tag{1}$$

with $\rho_{\mathrm{elec},\,m}$ and I_{m} as the electron density and the mean ionisation energy, respectively, with m as the index for the material under investigation or water, β as the proton velocity relative to the speed of light c, m_e as the electron mass, and ignoring density and shell corrections. We assume a proton energy of 200 MeV, noting that the energy dependency of the SPR value is very small in this energy range (in the order of 0.005% between 10 and 250 MeV).

The mean ionisation energy I of a compound is determined by combining the ionisation energies of its elemental constituents using Bragg's additivity rule, neglecting the influence of chemical binding energies:

$$\ln(I) = \left(\sum_p \frac{w_p Z_p}{A_p}\ln(I_p)\right)\left(\sum_p \frac{w_p Z_p}{A_p}\right)^{-1}\quad , \tag{2}$$

with the weight fraction w_p , atomic number Z_p , atomic weight A_p and the ionisation energy I_p of element p. Values for the elemental ionisation energies are taken from ICRU report 49 (International Commission on Radiation Units and Measurements 1993), applying the rule by Seltzer and Berger (1982) which is to use I-values that are 13% larger than the I-values for elemental substances in the condensed phase (except for the elements H, C, N, F and Cl; see also section A.2 in the supplementary material).

2.4. CRLB formalism

For a comprehensive description of the CRLB formalism we refer to the book by Kay (1993); here, we summarise the aspects relevant to this work, following mostly the notation therein.

We assume that the k measurements $\boldsymbol{x}$—which denote either the deposited energy in the detector (for setups using EIDs) or the number of photons in different energy bins (for setups using PCDs)—follow a k-dimensional multi-variate normal probability density function, i.e.

$$f(\boldsymbol{x}|\boldsymbol{\theta}) = (2\pi)^{-k/2}\ \det\left[\boldsymbol{\Sigma}\left(\boldsymbol{\theta}\right)\right]^{-1/2}\ \exp\left(-\frac{1}{2}\left(\boldsymbol{x}-\boldsymbol{m}\left(\boldsymbol{\theta}\right)\right)^{\mathrm{T}}\boldsymbol{\Sigma}\left(\boldsymbol{\theta}\right)^{-1}\left(\boldsymbol{x}-\boldsymbol{m}\left(\boldsymbol{\theta}\right)\right)\right). \tag{3}$$

Here, $\boldsymbol{\theta} = [\rho_{\mathrm{elec},\,m}\ \ I_{\mathrm{m}}]^{\mathrm{T}}$ denotes the underlying material properties on which x-ray transmission depends, while $\boldsymbol{m}(\boldsymbol{\theta})$ and $\boldsymbol{\Sigma}(\boldsymbol{\theta})$ are the mean and covariance matrix of the measurements, respectively. From these measurements, we wish to estimate SPR($\boldsymbol{\theta}$). The CRLB provides the lower bound on the variance of any unbiased estimator of SPR of material m for the given object geometry:

$$\begin{aligned}\mathrm{Var}(\mathrm{SPR}) \geqslant &\left(\frac{\partial \mathrm{SPR}(\boldsymbol{\theta})}{\partial \rho_{\mathrm{elec},\,m}}\right)^2 \left[\mathbf{F}^{-1}(\boldsymbol{\theta})\right]_{00} + \left(\frac{\partial \mathrm{SPR}(\boldsymbol{\theta})}{\partial I_{\mathrm{m}}}\right)^2 \left[\mathbf{F}^{-1}(\boldsymbol{\theta})\right]_{11} \\ &+ \left(\frac{\partial \mathrm{SPR}\left(\boldsymbol{\theta}\right)}{\partial \rho_{\mathrm{elec},\,m}} \cdot \frac{\partial \mathrm{SPR}\left(\boldsymbol{\theta}\right)}{\partial I_{\mathrm{m}}}\right) \cdot \left(\left[\mathbf{F}^{-1}\left(\boldsymbol{\theta}\right)\right]_{01} + \left[\mathbf{F}^{-1}\left(\boldsymbol{\theta}\right)\right]_{10}\right).\end{aligned} \tag{4}$$

In the following, we denote the lower bound on Var(SPR), as given by the CRLB formalism, simply as CRLB.

The derivatives of SPR with respect to $\rho_{\mathrm{elec},\,m}$ and I_{m} can be calculated analytically using equation (1). The elements of the Fisher information matrix $\mathbf{F}(\boldsymbol{\theta})$ can be calculated according to (Kay (1993), equation (3.31))

$$\left[\mathbf{F}\left(\boldsymbol{\theta}\right)\right]_{ij} = \left[\frac{\partial \boldsymbol{m}\left(\boldsymbol{\theta}\right)}{\partial \theta_i}\right]^{\mathrm{T}} \boldsymbol{\Sigma}^{-1}\left(\boldsymbol{\theta}\right) \left[\frac{\partial \boldsymbol{m}\left(\boldsymbol{\theta}\right)}{\partial \theta_j}\right] + \frac{1}{2}\mathrm{tr}\left[\boldsymbol{\Sigma}^{-1}\left(\boldsymbol{\theta}\right)\frac{\partial \boldsymbol{\Sigma}\left(\boldsymbol{\theta}\right)}{\partial \theta_i}\boldsymbol{\Sigma}^{-1}\left(\boldsymbol{\theta}\right)\frac{\partial \boldsymbol{\Sigma}\left(\boldsymbol{\theta}\right)}{\partial \theta_j}\right]. \tag{5}$$

The partial derivatives $\partial \boldsymbol{m}(\boldsymbol{\theta})/\partial\theta_i$ and $\partial \boldsymbol{\Sigma}(\boldsymbol{\theta})/\partial\theta_i$ are obtained by varying the electron density or ionisation energy of the material (section 2.5). For the resulting object composition, we calculate the expected number of primary photons arriving at the detector analytically based on the Lambert–Beer law, adding a (cross-)scatter component obtained from MC simulations (section 2.7, figure 2). After the application of a detector response function (section 2.8), the spectrum is then either binned (in case of PCDs) or the deposited energy is calculated (in case of EIDs), and the mean and variance of the resulting quantities are calculated. Finally, the derivative of the mean and variance are calculated w.r.t. $\boldsymbol{\theta}$. To reduce the computational burden, we calculate the CRLB for a selected subset of lines only (as indicated in figure 2, box 'Analytical calculation'), combining the CRLB values of this subset of lines. An illustration of the workflow is shown in figure 2; for details on this and the implementation of the CRLB calculation we refer to section A.1 in the supplementary material.

Please note that the CRLB methodology only provides a lower bound on the variance with which SPR can be estimated, but it neither yields SPR values, neither does it provide an estimator that can reach the theoretical CRLB limit, nor does it make a statement if such an estimator even exists.

2.5. Object and material definitions, setup geometry

In case of MC simulations of scatter or deposited dose, we define the phantom as a homogeneous object with a composition approximating the average composition of humans (figure 2, box 'MC simulation').

For the analytical calculation of primary x-rays arriving at the detector, we use a two-compartment model consisting of soft tissue and bone, whose combined composition equals the homogeneous composition used for MC simulations. As a consequence of this choice, the two-compartment model uses a constant ratio of the ray length through soft tissue to the ray length through bone for every ray crossing the phantom (figure 2, box 'Analytical calculation'). A two-compartment model allows us to apply the CRLB to SPR extraction of either soft tissue or bone by varying the material parameters of either of them. In order to estimate $\partial \boldsymbol{m}(\boldsymbol{\theta})/\partial\rho_{\mathrm{elec},m}$ and $\partial \boldsymbol{\Sigma}(\boldsymbol{\theta})/\partial\rho_{\mathrm{elec},m}$ the mass density of either soft tissue or bone is varied in steps of 1 %, and in order to estimate $\partial \boldsymbol{m}(\boldsymbol{\theta})/\partial I_{\mathrm{m}}$ and $\partial \boldsymbol{\Sigma}(\boldsymbol{\theta})/\partial I_{\mathrm{m}}$ the composition of either soft tissue or bone is changed such that the ionisation energy varies in steps of (1.0000 ± 0.0001) eV. For further details on

elemental compositions, mass densities and weight fractions of the simulated materials as well as their variation we refer to section A.2 in the supplementary material.

As shown in section B.1 of the supplementary material, the optimisation of setup parameters depends on whether one optimises for the extraction of SPR of bone or of soft tissue. However, the best performing settings for the two tissues differ by such a small margin (e.g. less than 1 keV in case of a single-source setup with a PCD with 2 bins) that in this work we focus on the extraction of SPR of soft tissue only.

The simulated CBCT geometry (figure A.2 in the supplementary material) mimics a typical CBCT setup integrated into a proton radiotherapy gantry with a source-isocentre distance of 2300 mm and an isocentre-detector distance of 900 mm. The phantom is simulated as a cylinder with a diameter and height of both 330 mm. The size of the phantom is based on standard image quality phantom sizes, which in turn are based on average patient sizes.

2.6. X-ray spectra and deposited dose

We obtain x-ray spectra from SpekCalc (Poludniowski *et al* 2009) for a tungsten target and an anode angle of 7° with energy steps of 1 keV (see figures A.4 to A.7 in the supplementary material). The intrinsic source filtration is assumed to be 0.8 mm Be and 0.89 mm Ti. For further beam hardening, 0.2, 0.4, 0.6, 0.8 mm of tin are investigated.

For a fair comparison between all setups and acquisition settings, we keep the cumulative dose deposited in the phantom constant at an arbitrary value of $(1.24426 \pm 0.00046) \cdot 10^{16}$ MeV. As discussed in the supplementary material, section B.1, the chosen value of the cumulative reference dose does not have any influence on the optimisation result. The deposited dose per number of emitted photons from the source is determined using MC simulations as described in section 2.7.

2.7. X-ray scatter originating in the phantom

We use MC simulations using 3.6×10^{10} primaries to obtain the x-ray scatter caused by the phantom for a given source voltage and filtration, based on the setup described in section 2.5. The MC simulations are implemented using GATE (version 9.2) (Sarrut *et al* 2014) which is based on the Geant4 toolkit (version 11.0.0) (Allison *et al* 2016).

In order to obtain the scatter component, the photons intersecting the detector plane are split into scattered and non-scattered photons based on their trajectory. For registration of cross-scatter between two orthogonal source-detector pairs, a second detector plane is placed at the same isocentre-detector distance as the first detector plane, but perpendicular to the axis between source and first detector plane (see figure 2, box 'MC simulation').

The MC data of primary photons and (cross-)scatter contributions are stored as histograms of the number of photons per energy bin, using energy bins of 1 keV width. The data are then smoothed using a two-dimensional Gaussian kernel in the spatial domain. The (cross-)scatter data is finally normalised to the number of primary photons.

Our algorithm for determining the CRLB calculates the primary component analytically in steps of 1 keV and subsequently adds the MC-based scatter as well as, if applicable, cross-scatter components, yielding the total expected number of photons arriving at the detector in steps of 1 keV. It is assumed that the volume spanned by the source and a given detector pixel is negligibly small compared to the irradiated volume of the phantom. As a result, when the number of primaries changes due to a variation of the line integral between the source and that pixel, either due to a variation in electron density or composition to calculate the derivatives in equation (5), then the number of scattered and cross-scattered photons stays constant.

The variance of the smoothed (cross-)scatter component and its influence on the resulting CRLB values is negligible with relative standard deviations $\leqslant 0.2\%$; as a consequence, we do not report the standard deviation on obtained CRLB values. For more information see section B.2 in the supplementary material.

2.8. Detector response function

When modelling ideal detectors in our simulation study, it is assumed that the detection efficiency is 100%, that inter-pixel cross-talk, electronic noise and pile-up are all absent, and, as a result, that the spectrum of registered events equals the spectrum of incoming photons.

When modelling realistic detectors in our simulation study, the spectrum of deposited events is determined based on x-ray transport detector response functions. These x-ray transport detector response functions, specific for the layer compositions and layer thicknesses stated above, are obtained using MC simulations in Gate (see section 2.7) by irradiating the centre pixel of a grid of pixels (without dead-space between the pixels) with monoenergetic beams and registering the spectrum of events deposited in the centre pixel, the spectrum of events deposited in all surrounding pixels, and the spectrum of events leaving the detector downstream from the source.

For realistic EIDs it is then assumed that the spectrum of registered events equals the spectrum of deposited events. For realistic PCDs, however, the spectrum of deposited events obtained from the x-ray transport simulations is used as input for a charge sharing model unless explicitly stated otherwise, based on an isotropic 3D-Gaussian distribution (Taguchi *et al* 2018) with a charge cloud size of $\sigma = 30\,\mu$m, independent of deposited energy (Stierstorfer 2018). The output of the charge sharing model is subsequently used as the spectrum of registered events. The pixel size for both simulation of x-ray cross-talk and charge sharing is $300 \times 300\,\mu\text{m}^2$ for both EIDs and PCDs, which is similar to the pixel cross-section of commercially available PCD CT scanners (Rajendran *et al* 2022, Marsh *et al* 2023, McCollough *et al* 2023).

It is noted that our model of realistic detectors does not include effects degrading the energy resolution apart from those described above. For example, neither electronic noise nor pulse pile-up are included.

For more details we refer to section A.3 in the supplementary material.

3. Results

3.1. Optimisation of setups based on an ideal detector response function

In the following, we present the results for the optimisation of spectral CBCT implementations assuming an ideal detector response function, with the lowest possible variance on SPR as given by the CRLB as our figure of merit (lower is better); for a summary see table 2 and figure 4. Note that x-ray scatter originating from the phantom and, if applicable, cross-scatter between two source-detector pairs is included.

3.1.1. Single-source setup with ideal PCD

Higher source voltages prove to be beneficial for this setup. A source voltage of 140 kVp without additional source filtration yields the best results regardless of the number of energy bins used by the PCD. In the limit of a near-continuous binning with bins of 1 keV width (table B.5), the lowest (i.e. best) CRLB value across all setups, source voltages and filtrations is achieved and hence used as a reference value. All CRLB values in this work are reported as normalised CRLB values (nCRLB) relative to this reference value, regardless of whether an ideal or realistic detector model is considered.

Using a limited number of two (table B.2 and figure 4(a), three or four (table B.3 and B.4) bins only, nCRLB values of 1.31, 1.16 and 1.11 are reached (table 2).

3.1.2. Single-source setup with ideal dual-layer detector

Across all source voltages, all Sn source filtration thicknesses for 140 kVp, and without an additional filtration layer bin, the lowest nCRLB value of 1.25 is achieved for 140 kVp without additional source filtration (figure 4(b) and table B.6). Adding a filtration layer bin with a width of 16 keV lowers the nCRLB further by 8% to a value of 1.16 (figure B.6).

3.1.3. Single rapid voltage-switching source with ideal EID

For all possible source voltage combinations between 80 kVp and 140 kVp without additional source filtration, the 80/140 kVp voltage pair performs best (table B.7 and figure B.7). Additional Sn source filtration applied to the 80/140 kVp voltage pair affects both the LE and HE spectrum simultaneously (figure 4(c)). The lowest nCRLB value of 1.62 is achieved for a filtration of 0.8 mm Sn, however, this optimum is achieved for a very high mAs ratio of $\text{mAs}_{\text{LE}} : \text{mAs}_{\text{HE}} = 29 : 1$. Examining the results not as a function of mAs ratio but as a function of the ratio between the number of photons emitted (including source filtration) during the LE or HE phase (figure B.22(a)) shows that the minimum nCRLB value is always reached in the vicinity of a photon number ratio of 1 : 1, i.e. equal number of photons emitted during the LE and HE phase. The high value of 29 : 1 for the optimum mAs ratio for a 80/140 kVp spectrum combination filtered by 0.8 mm of tin hence counteracts the influence of stronger filtration on the LE spectrum.

In case we assume that the rapid switching source can only switch between voltages, but not between mAs levels (i.e. $\text{mAs}_{\text{LE}} : \text{mAs}_{\text{HE}} = 1 : 1$), the lowest nCRLB of 5.65 is achieved using a 0.2 mm Sn filtration (table 2). This result is more than three times worse than that obtained with the optimised mAs ratio, emphasising the importance of optimising both voltages and mAs levels. Moreover, depending on the mAs ratios achievable with a realistic switching source, a different filtration might perform best.

3.1.4. Dual-source setup with two ideal EIDs

Comparing different voltage pairs, the 100/140 kVp voltage pair performs best for $\text{mAs}_{\text{LE}} : \text{mAs}_{\text{HE}} \leqslant 2.5 : 1$, whereas the 80/140 kVp voltage pair achieves the lowest nCRLB values for larger mAs ratios (figure B.9).

We observe the same trends regarding filtration for both the 80/140 kVp and the 100/140 kVp voltage pair: adding Sn filtration to only the LE spectrum does not lower the nCRLB compared to the unfiltered spectra (figure B.10 and B.13). Adding Sn filtration to only the HE spectrum lowers the nCRLB significantly,

Table 2. Results for the optimisation of various spectral CBCT setups w.r.t. the extraction of SPR, assuming an ideal detector response function. The table lists the settings yielding the lowest nCRLB for each setup as well as additional entries of interest.

Setup	Spectrum (combination)	Parameters (bins, $mAs_{LE}:mAs_{HE}$)	Min. nCRLB
Single-source setup with PCD	140 kVp	[20, 76, 140] keV	1.31
	140 kVp	[20, 70, 94, 140] keV	1.16
	140 kVp	[20, 60, 75, 95, 140] keV	1.11
	140 kVp	Continuous binning	1.00
Single source with dual-layer detector	140 kVp	[20, 72, 140] keV	1.25
	140 kVp	[20, 68, 84, 140] keV	1.16
kVp-switching setup with EID	80 kVp, 0.2 mm Sn/ 140 kVp, 0.2 mm Sn	1 : 1	5.65
	80 kVp, 0.8 mm Sn/ 140 kVp, 0.8 mm Sn	29 : 1	1.62
Dual-source setup with EIDs	80 kVp/ 140 kVp, 0.8 mm Sn	1.75 : 1	2.92
kVp-switching setup with PCD	80 kVp/140 kVp	1:1; LE bins: [20, 60, 80] keV, HE bins: [20, 75, 140] keV.	1.31
	80 kVp, 0.2 mm Sn/ 140 kVp, 0.2 mm Sn	3.5 : 1; LE bins: [20, 65, 80] keV, HE bins: [20, 85, 140] keV.	1.23
Dual-source setup with PCDs	80 kVp/140 kVp	HE only; HE bins: [20, 75, 140] keV.	1.31
	80 kVp/ 140 kVp, 0.8 mm Sn	1.75 : 1; LE bins: [20, 60, 80] keV, HE bins: [20, 90, 140] keV.	1.30

with stronger filtration yielding lower nCRLB values (figure B.11 and B.14) while shifting the minimum towards lower values of $mAs_{LE}:mAs_{HE}$. Adding the same thickness of Sn filtration to both the LE and HE spectra decreases the nCRLB values as well, but shifts the minimum to larger mAs ratios (figure B.12 and B.15) and is still outperformed by applying filtration to the HE spectrum only.

The lowest nCRLB value of 2.92 is reached by a 80/140 kVp voltage pair with 0.8 mm Sn filtration added to the 140 kVp spectrum only, and a mAs ratio of $mAs_{LE}:mAs_{HE} = 1.75:1$ (figure 4(d) and table B.8). Similarly to the kVp-switching setup, we observe that, while the optimum mAs ratios for the various filtration settings differ considerably, their corresponding ratios between the number of photons emitted by the LE and HE source are between 1 : 1 and 5 : 1 (figure B.22(b)). Hence, large mAs ratios counteract the stronger effect of filtration on the LE spectrum also in this setup.

3.1.5. Single rapid voltage-switching source with ideal PCD

Comparing all possible source voltage combinations between 80 and 140 kVp without additional source filtration (figure B.16), we see that while the mean nCRLB value of the 120/140 kVp voltage pair, averaged over the whole investigated mAs ratio range, is lowest, it is always outperformed by the 80/140 kVp voltage pair for $mAs_{LE}:mAs_{HE} \leqslant 5:1$. The lowest nCRLB is achieved in the limit of very low mAs ratios for all source voltage combinations, that is, in the limit that only the HE phase of the source is used (table B.9).

As soon as filtration is added to the 80/140 kVp spectrum combination, affecting both the LE and HE spectrum simultaneously, the minimum CRLB is found in the regime of mAs ratios where both the LE and HE phase of the source are used. The lowest nCRLB value of 1.23 is achieved for a filtration of 0.2 mm Sn at a mAs ratio of $mAs_{LE}:mAs_{HE} = 3.5:1$. If the mAs ratio is fixed at $mAs_{LE}:mAs_{HE} = 1:1$, the nCRLB value increases to 1.31 using no additional source filtration. Hence, depending on the mAs ratios achievable with a realistic source, a different filtration might perform best (figure 4(e)).

3.1.6. Dual-source setup with two ideal PCDs

The investigation of different voltage pairs shows the same behaviour as for the kVp-switching counterpart, with the only difference that the 80/140 kVp voltage pair outperforms the 120/140 kVp voltage pair for a mAs ratio of $mAs_{LE}:mAs_{HE} \leqslant 3.5:1$.

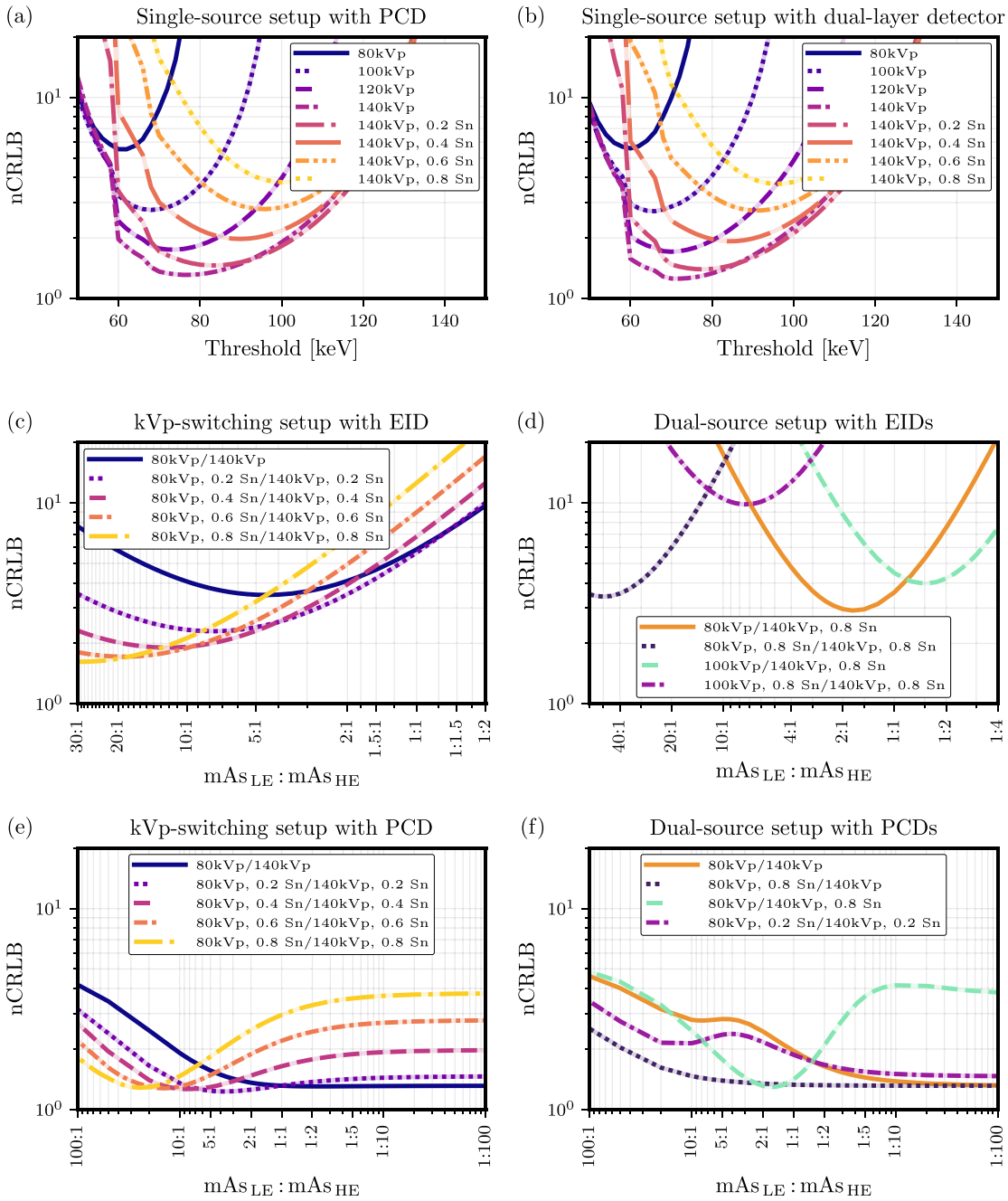

Figure 4. Examples of optimisation of spectral CBCT setups w.r.t. the extraction of SPR, assuming an ideal detector response function. Single-source setup with (a) a PCD with two energy bins and (b) a dual-layer detector without filtration bin, optimising the threshold between the low and high energy bins. (c) kVp-switching setup with one EID and (d) dual-source setup with two EIDs, optimising the ratio $\mathrm{mAs_{LE}}:\mathrm{mAs_{HE}}$ between the LE and HE spectra. (e) kVp-switching setup with one PCD and (f) dual-source setup with two PCDs; for each mAs ratio, the minimum nCRLB of all tested threshold combinations is plotted. All values are reported as normalised CRLB values as stated in the text with the same nCRLB value range for all figures; source filtration is specified in millimetres of tin.

For the 80/140 kVp voltage pair, adding filtration to only the LE spectrum lowers the nCRLB in the regime of mAs ratios where both sources are active, but the lowest nCRLB values are still achieved in the limit that only the HE source is active (figure B.19).

In the cases that only the HE spectrum is filtered or that the same filtration is added to both sources, the simultaneous utilisation of both sources yields nCRLB values that are lower than those obtained with only the HE source, provided that stronger filtration is used. For the combination of 80 kVp/140 kVp with a strong HE filtration of 0.8 mm Sn, the lowest overall nCRLB value for this setup of 1.30 is achieved using a mAs ratio of $\mathrm{mAs_{LE}}:\mathrm{mAs_{HE}} = 1.75:1$ (figure B.21).

The best performing settings for each of the different filtration cases (no filtration, only LE filtration, only HE filtration, and both LE and HE filtration) are compared in figure 4(f) (see also table B.11).

Table 3. Results for the optimisation of various spectral CBCT setups w.r.t. the extraction of SPR, assuming a realistic detector response function. The table lists the settings yielding the lowest nCRLB for each setup as well as additional entries of interest.

Setup	Spectrum (combination)	Parameters (bins, mAs_{LE} : mAs_{HE}, layer thicknesses)	Min. nCRLB
Single-source setup with PCD	140 kVp	[20, 70, 140] keV	3.96
	140 kVp	[20, 68, 88, 140] keV	3.62
	140 kVp	[20, 60, 70, 90, 140] keV	3.45
	140 kVp	Continuous binning	3.14
Single source with dual-layer detector	140 kVp	Top layer: 0.45 mm CsI, bottom layer: 1.45 mm CsI.	11.6
	140 kVp	Top layer: 0.2 mm CsI, filtration layer: 1.8 mm Cu, bottom layer: 1.7 mm CsI.	7.78
kVp-switching setup with EID	80 kVp, 0.2 mm Sn/ 140 kVp, 0.2 mm Sn	1 : 1	9.46
	80 kVp, 0.8 mm Sn/ 140 kVp, 0.8 mm Sn	26 : 1	2.74
Dual-source setup with EIDs	80 kVp/140 kVp, 0.8 mm Sn	1.5 : 1	4.97
kVp-switching setup with PCD	80 kVp/140 kVp	1:1; LE bins: [20, 65, 80] keV, HE bins: [20, 70, 140] keV.	3.60
		20 : 1;	2.81
	80 kVp, 0.8 mm Sn/ 140 kVp, 0.8 mm Sn	LE bins: [20, 30, 80] keV, HE bins: [20, 80, 140] keV.	
Dual-source setup with PCDs	80 kVp/140 kVp	HE only; HE bins: [20, 70, 140] keV.	3.96
	80 kVp/ 140 kVp, 0.8 mm Sn	1.5 : 1; LE bins: [20, 65, 80] keV, HE bins: [20, 70, 140] keV.	3.27

3.1.7. Setups based on ideal detector response function: summary

Comparing all spectral CBCT implementations based on an ideal detector response function (table 2), excluding the reference PCD with near-continuous binning, the setup using a single source and a PCD with four energy bins performs best (nCRLB = 1.11), closely followed by a single-source setup using an ideal dual-layer detector and three effective bins (nCRLB = 1.16) and a single-source setup using a PCD with three energy bins (nCRLB = 1.16), with an increase in nCRLB by 4.5%. A dual-source setup with two PCDs with two energy bins each (nCRLB = 1.30) performs only slightly better than a single-source setup with a PCD with two energy bins (nCRLB = 1.31), but worse than a kVp-switching setup with a PCD with two energy bins for each phase (nCRLB = 1.23), which in turn performs worse than a single source setup with a PCD with four energy bins. The performance of setups using EIDs is worse compared to setups using any other type of detector: the kVp-switching setup with one EID reaches a nCRLB value of 1.62, whereas the dual-source setup with two EIDs is additionally affected by cross-scatter and reaches a nCRLB value of 2.92.

Under the assumption that the rapid switching source can only switch between voltages but not mAs levels, the kVp-switching setup with a PCD performs slightly worse (nCRLB = 1.31) than a dual-source setup with two PCDs (nCRLB = 1.30). For the kVp-switching setup using an EID, however, the deterioration is much more pronounced, leading to a nCRLB of 5.65, which is the worst out of all spectral CBCT configurations with ideal detectors.

3.2. Optimisation of setups based on a realistic detector response function

The optimisation of setups using a realistic detector response function is performed analogously to the optimisation of setups using an ideal detector response function; a summary thereof can be found in table 3. We observe that for each individual spectral CBCT setup, the trends in performance w.r.t. the optimised parameters are similar for both an ideal and realistic detector response function. Due to this similarity, here we only summarise the results and refer the interested reader to the supplementary material, section B.4, for details on the results for the optimisation of setups using a realistic detector response function.

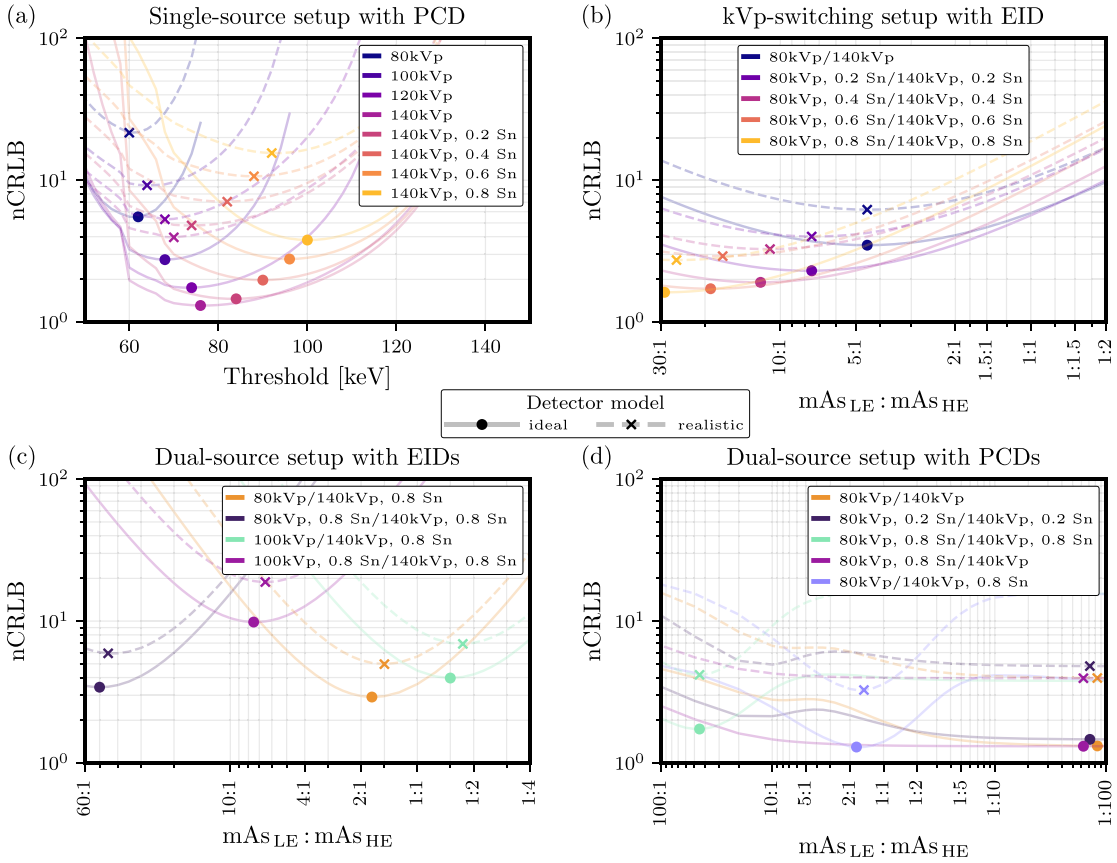

Figure 5. Comparison of spectral CBCT setups optimised w.r.t. the extraction of SPR, assuming either an ideal or a realistic detector response function. Markers indicate the position of optima. (a) Single-source setup with one PCD using two energy bins, optimising the threshold between the low and high energy bin. (b) kVp-switching setup with EID and (c) dual-source setup with two EIDs, optimising the ratio $mAs_{LE} : mAs_{HE}$ between the LE and HE spectra. (d) Dual-source setup with PCDs; for each mAs ratio, the minimum nCRLB of all tested threshold combinations is plotted; markers at a mAs ratio of 1 : 100 indicate that the best performance is reached in the limit of using the HE source only; overlapping markers are slightly offset for better readability. All values are reported as normalised CRLB values as stated in the text; source filtration is specified in millimetres of tin.

3.2.1. Setups based on realistic detector response function: summary

Comparing all spectral CBCT implementations based on a realistic detector response function (table 3), excluding the PCD with near-continuous binning, the single-source setup with a dual-layer detector performs worst out of all setups (nCRLB = 7.78, with filtration layer), unless the source of the kVp-switching setup with one EID is limited to a mAs ratio of 1 : 1 in which case this setup has worst performance (nCRLB = 9.46). In contrast, if the kVp-switching setup with one EID uses a source that can reach any mAs ratio, it performs best out of all setups (nCRLB = 2.74), closely followed by a kVp-switching source combined with a PCD (nCRLB = 2.81). Similarly, limiting the kVp-switching setup with one PCD to a mAs ratio of 1 : 1 causes it to perform worse (nCRLB = 3.60) than the dual-source setup with PCDs (nCRLB = 3.27). The dual-source setup with two PCDs (nCRLB = 3.27) now performs better than a single-source setup with a PCD with either two, three or even four energy bins (nCRLB of 3.96, 3.62 and 3.45, respectively). In comparison to the kVp-switching setups capable of any mAs ratio, the dual-source setups again perform worse (nCRLB = 4.97 using EIDs, nCRLB = 3.27 using PCDs) due to the influence of cross-scatter.

3.3. Comparison of setups using either an ideal or realistic detector response function

Figure 5 compares the performance of spectral CBCT setups using either an ideal or realistic detector response function. As mentioned before, the trends are largely the same w.r.t. the optimised parameters for individual setups, with the assumption of a realistic detector response function yielding consistently worse results.

Comparing the difference in optimum performance assuming either ideal or realistic detectors, the nCRLB of a single-source setup with a realistic PCD is about a factor of 3.0 to 3.1 larger than in the ideal case, about a factor of 2.3 for a kVp-switching setup with one PCD, and about a factor of 2.5 for a dual-source setup with PCDs. For the setups based on one or two EIDs, the performance of realistic setups deteriorates by a smaller factor of about 1.7 compared to ideal setups. For a single-source setup with a dual-layer detector,

the ideal and realistic setup differ in performance by a factor of 9.2 without and a factor of 6.7 with filtration between the detector layers/bins.

4. Discussion

4.1. Comparison of setups

When assuming a realistic detector response function, we observe that the optimal threshold settings are shifted towards lower energies compared to their ideal detector counterparts for the case of a single-source setup with a PCD with either two (figure 5(a)), three or four bins (tables 2 and 3). This could be due to the shift of the spectrum of registered events to lower energies in the case of a realistic detector response function (figure 6(a)), which is a consequence of x-ray cross-talk and charge sharing.

For the kVp-switching setup combined with an EID as well as for the dual-source setup with EIDs, we observe that the optimum current ratio is shifted towards the HE source spectrum when assuming a realistic detector response function, compared to their ideal counterparts (figures 5(b) and (c)). A possible contribution to this behaviour could be that, when changing from an ideal to a realistic detector response function, the deposited energy during the LE phase is reduced by −6.6% in the example shown in figures 6(c) and (d) (values for centre pixel of detector only), whereas the deposited energy during the HE phase is reduced by −25%. An increase of the HE source current for the realistic setups would counteract the change in the ratio of deposited energy to some extent.

Comparing ideal and realistic setups, the degradation in performance is largest for the dual-layer setup. The good performance of an ideal dual-layer detector is due to its perfect separation of the registered spectrum into two energy bins (three with filtration) combined with a readout in the fashion of an EID; however, for the realistic dual-layer detector the spectral separation between the spectra registered by the top and bottom layer is relatively poor (see figure 6(b)).

Generally, we observe that a higher source voltage or a larger spectral separation between the source spectra leads to better SPR extraction. For example, when comparing all possible voltage pairs between 80 kVp and 140 kVp, the 80/140 kVp voltage pair usually performs best. Another example illustrating this point particularly well is the comparison between an ideal PCD with two energy bins and an ideal dual-layer detector with two effective energy bins, both paired with a single source: The dual-layer detector assigns a stronger weight to HE photons and achieves a better performance. Both setups show equal performance when using three instead of two bins, even despite the dual-layer detector's third filtration bin discarding all photons falling into this bin (140 kVp, 2 bins: nCRLB = 1.25 for dual-layer detector, nCRLB = 1.31 for PCD; 140 kVp, 3 bins: nCRLB = 1.16 for both dual-layer detector and PCD).

A comparison between kVp-switching and dual-source setups shows that the kVp-switching setups perform better; this holds true for both the case of an ideal and realistic detector response function, and for both the case of using EIDs or PCDs as detectors. Given the same source spectra and source filtration, cross-scatter is the only difference between kVp-switching and dual-source setups in our model and therefore the reason for their difference in performance. For example, if we compare the kVp-switching setup with one EID to the dual-source setup with two EIDs for the same operating conditions of an unfiltered spectrum combination of 80/140 kVp, a mAs ratio of $\mathrm{mAs_{LE}} : \mathrm{mAs_{HE}} = 6.5 : 1$ and an ideal detector response, then the addition of cross-scatter causes a 2.6 fold increase in the CRLB values for the dual-source setup compared to the kVp-switching setup (see also figures B.42 and B.43 for a comparison between kVp-switching and dual-source setups based on EIDs). The absence of cross-scatter is hence the reason for the better performance of the kVp-switching setups, despite their limitations when it comes to the choice of source filtrations. It should be noted, however, that kVp-switching setups only outperform their dual-source counterparts as long as an ideal source capable of reaching any mAs ratio is assumed; we refer to the discussion in section 4.3 for more on this.

Comparing the difference in performance between setups based on either ideal or realistic PCDs, the nCRLB for the kVp-switching and the dual-source setup degrades less (by a factor of 2.3 and 2.5, respectively) compared to a single-source setup (by a factor between 3.0 and 3.1, depending on the number of bins), since the use of two distinct source spectra can counteract the deterioration of spectral response in the detector. In contrast to this, a realistic detector response function degrades the nCRLB of setups based on EIDs by a factor of only 1.7; hence, the degradation is more severe for PCDs, and consequently there are greater gains possible by improving the performance of (realistic) PCDs. We attribute the more severe deterioration in the case of PCDs to the additional cross-talk caused by charge sharing, which degrades their spectral performance. If charge sharing is neglected and only x-ray transport is included in the detector response function, then in case of a single-source setup with a PCD the nCRLB is only increased by a factor of about 2.0–2.1 relative to the results based on an ideal detector response function (see supplementary material, figure B.47 and tables B.22–B.25), compared to a factor of 3.0 to 3.1 if charge sharing is included on

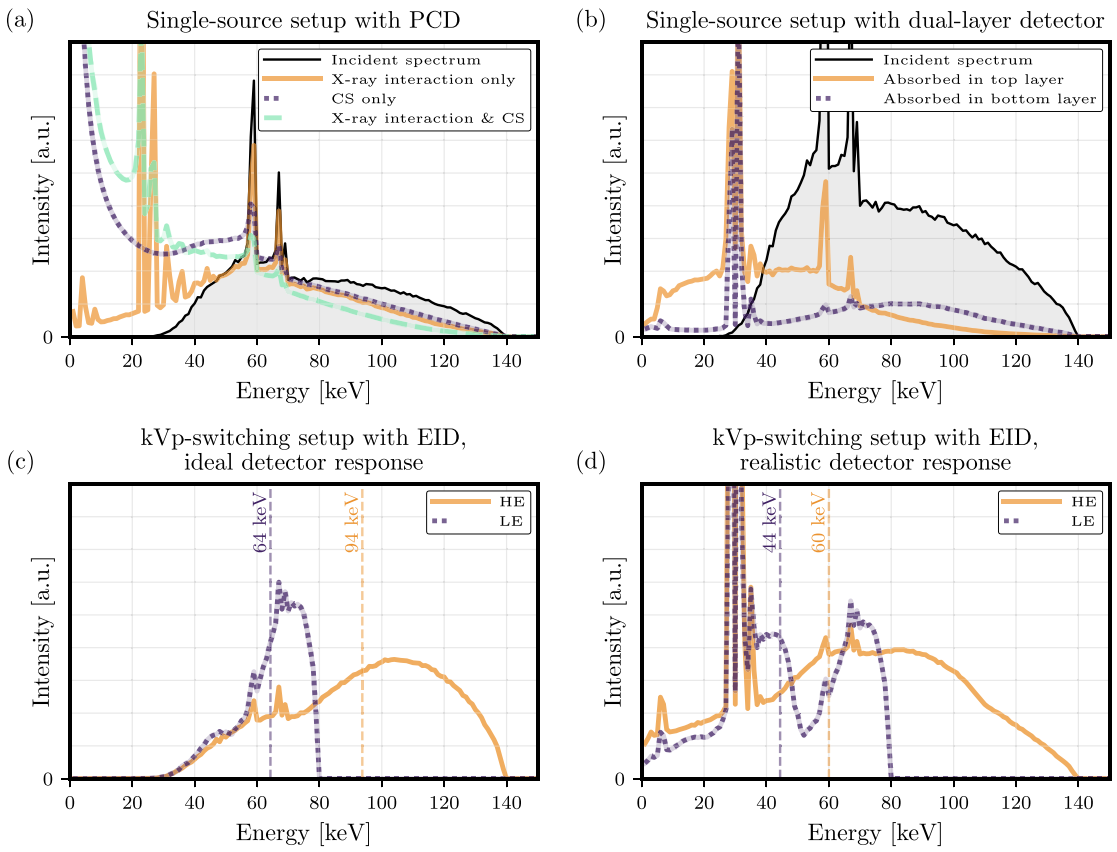

Figure 6. (a) Spectrum incident on a PCD as well as the spectrum of events created in a pixel taking into account only x-ray interaction, only charge sharing (CS), or both x-ray interaction and charge sharing (centre pixel of detector, 140 kVp source spectrum). (b) Spectrum incident on a dual-layer detector as well as the spectra of events absorbed in the top and bottom layer (centre pixel of detector, 140 kVp source spectrum, 0.2 mm CsI top layer, 1.8 mm Cu filtration layer, 1.7 mm CsI bottom layer). (c), (d) Spectra of events created in the detector in case of a kVp-switching source combined with an ideal (c) and a realistic (d) EID, during either the low or high energy phase (centre pixel of detector, 80 kVp, 0.8 mm Sn/140 kVp, 0.8 mm Sn spectrum combination, $\mathrm{mAs}_{\mathrm{LE}} : \mathrm{mAs}_{\mathrm{HE}} = 27.5 : 1$). The horizontal lines mark the mean energy of each spectrum. The value range of the *y*-axes is set individually for each figure to show relevant features more clearly.

top of x-ray transport. This translates to an improvement of CRLB values by 32%–35% when charge sharing is neglected, compared to the case of including both x-ray transport and charge sharing. These results are in line with a work published by Taguchi and us, indicating that indirect-conversion PCDs, which do not suffer from charge sharing, may offer better performance than PCDs based on CdTe or CZT in spectral imaging tasks such as water-bone decomposition or K-edge imaging (Taguchi *et al* 2025). Similarly, indirect-conversion PCDs may be better suited for the task of SPR determination investigated here.

Concerning the future development of spectral CBCT for adaptive proton therapy, we would like to note that dual-source setups with EIDs are already available in some proton gantries, while the installation of rapid switching x-ray sources seems feasible. While our results based on an ideal detector response function suggest that both these setups are outperformed by a single-source setup with a PCD (table 2), our results based on a realistic detector response function (table 3) show that a kVp-switching setup with an EID and an ideal source outperforms a dual-source setup with EIDs by a factor of 1.8, and a single-source setup with a PCD with four bins by a factor of 1.3. If the detector response function of PCDs is assumed to be based solely on x-ray transport, then a PCD with 4 bins (table B.24) outperforms the kVp-switching setup with an EID by a factor of 0.82. Hence, taking into account the currently available technology, a rapid switching source with an EID seems preferable. For future developments, we encourage the investigation of concepts for PCDs free of charge sharing, such as PCDs based on ultrafast scintillators (Van Der Sar *et al* 2021).

While we only focus on optimising and comparing spectral CBCT setups w.r.t. their performance for SPR extraction, the decision to implement one of the discussed variants should also take into account its performance w.r.t. soft tissue contrast, its sensitivity to patient motion, as well as its cost and feasibility. Dual-source setups will be more expensive than single-source setups, and setups based on an EID are likely to be cheaper than those including a PCD, with dual-layer detectors probably lying somewhere in between.

4.2. Limitations of the applied methodology

We do not include the effect of pulse pile-up on PCD performance. Addressing this concern, we would like to note that pile-up is most prominent for pixels for which the projection lines pass just below the surface of the object under investigation, and therefore exhibit the least attenuation. In our case, the photon flux for pixels in the centre is about 130 times lower, which decreases the probability of pile-up while it simultaneously causes an increase of CRLB values. Furthermore, we find that these pixels in the centre dominate the overall behaviour of the CRLB in our case. We therefore expect that pile-up does not significantly affect the trends we observe. Last but not least, we have estimated the fluence rate at the position of the detector to be one order of magnitude lower for CBCT compared to fan-beam CT (Sar and Schaart 2025).

While the CRLB gives the theoretical limit of performance, it does not state which estimator can reach this limit and if such an estimator exists. Moreover, the approach of comparing different spectral CBCT setups based on their CRLB can unfortunately not be extended to single-energy SPR estimation since SPR depends on the two variables ρ_{elec} and I. Consequently, our methodology cannot be used to compare the results based on spectral CBCT presented here to single-energy CBCT.

Furthermore, we cannot compare the CRLB values on SPR extraction we obtain with values reported in literature, since the CRLB values depend linearly on the number of photons emitted by the source. Without knowing this number precisely, a comparison to experimental values of variance on SPR cannot be drawn. Moreover, values reported in literature are mostly obtained using image-based methods and hence influenced by both the choice of reconstruction algorithm and the conversion scheme from HU to SPR values. Similarly, we cannot quantify the range uncertainty achievable with the setups investigated in this study. We therefore plan a follow-up simulation study to compare our CRLB approach to image-based methods.

One main difference between cone-beam CT and fan-beam CT is the increased scatter in CBCT. To give an intuition for how this affects performance, a selection of results without any (cross-)scatter can be found in section B.8 of the supplementary material.

4.3. Closing remarks

We observe that the performance of the source ultimately determines whether a kVp-switching or a dual-source setup performs better. In our simulation we assume an ideal kVp-switching source capable of instant and perfect transitions between source voltages and mAs levels, which in reality is not the case. However, we note that, first, we focus on gantry-mounted CBCT with rotation times in the order of 60 s, which therefore provides more time for switching voltages and currents. Current ratios of 4 : 1, and therefore mAs ratios, for a rapid switching source with a cycle frequency of 7.5 Hz were reported (Haytmyradov *et al* 2019). Second, a limited current-switching capability of a source can be mitigated by using different duty cycles for the LE and HE levels, assuming that the acquisition time of the detector can be adjusted accordingly. Using this technique, mAs ratios between 5.7 : 1 and 1 : 5.7 were reported for a clinical-grade fan-beam CT switching source (Sandvold *et al* 2024). Third, novel x-ray sources, such as those based on carbon nanotubes, could offer an alternative approach that also addresses the imperfect separation of voltage levels, moreover, they might offer greater flexibility in designing the source by being able to incorporate multiple focal spots into a compact housing with optional individual filtration (Xu *et al* 2023a, 2023b, Li *et al* 2024). This also offers the possibility of using an array of source focal spots to realise a more fan-beam-like geometry, reducing scatter and limiting reconstruction artefacts due to insufficient data (Spronk *et al* 2021, Hu *et al* 2024).

5. Conclusion

In this work, we compared different realisations of simulated spectral cone-beam CT with respect to their suitability for extracting proton SPRs. The investigated setups were as follows:

- A single x-ray source operating at a fixed voltage with a PCD,
- A single source operating at a fixed voltage with a dual-layer detector,
- A rapid voltage-switching source with an EID,
- A rapid voltage-switching source with a PCD,
- Two sources at different fixed voltages coupled with an EID each,
- Two sources at different fixed voltages coupled with a PCD each.

All setups were optimised w.r.t. their main operating parameters to allow for a fair comparison between them. The figure of merit was the lowest possible variance on SPR as given by the CRLB. We found that setups based on a single source benefit from the absence of cross-scatter, that a higher source voltage or a larger energy separation appear beneficial for the extraction of SPR, and that the effect of charge sharing in

direct-conversion PCDs strongly degrades the accuracy of SPR estimation. Assuming an ideal source and a realistic detector response, a kVp-switching setup coupled with an EID performs best, and a single-source setup based on a dual-layer detector performs worst.

Data availability statement

The data that support the findings of this study will be openly available following an embargo at the following URL/DOI: https://doi.org/10.4121/bd754669-5af8-4e2d-9a70-37ac56bd6674. Data will be available from 27 July 2025.

Acknowledgment

The authors would like to acknowledge the high-performance computing clusters provided by the ICT department of TU Delft. We would also like to thank Rolf Behling for fruitful discussions. D L would like to thank Dan Wang for help with the Cramér-Rao Lower Bound formalism. Furthermore, we would like to thank the open source software community for creating GATE, GEANT4, Jupyter, Numpy, Python, Uproot and all other open source software that was directly or indirectly used in this work.

Disclosures

D L is funded by Varian, a Siemens Healthineers Company, Grant Number 2018016.

Disclaimer

Preliminary results of this work were presented at the SPIE Medical Imaging Conference 2024, San Diego, California, United States (Leibold *et al* 2024), and at the 62nd Annual PTCOG Conference 2024, Singapore.

References

Allison J *et al* 2016 Recent developments in Geant4 *Nucl. Instrum. Methods Phys. Res. A* **835** 186–225
Alvarez R E and Macovski A 1976 Energy-selective reconstructions in x-ray computerised tomography *Phys. Med. Biol.* **21** 733–44
Bär E, Lalonde A, Royle G, Lu H-M and Bouchard H 2017 The potential of dual-energy CT to reduce proton beam range uncertainties *Med. Phys.* **44** 2332–44
Bolsi A, Peroni M, Amelio D, Dasu A, Stock M, Toma-Dasu I, Nyström P W and Hoffmann A 2018 Practice patterns of image guided particle therapy in Europe: a 2016 survey of the European particle therapy network (EPTN) *Radiother. Oncol.* **128** 4–8
Cai E Y, De Caro C, Treb K and Li K 2023 Benefits of using removable filters in dual-layer flat panel detectors *Phys. Med. Biol.* **68** 085013
Chen Z *et al* 2023 Proton versus photon radiation therapy: a clinical review *Front. Oncol.* **13** 1133909
Haytmyradov M *et al* 2019 Markerless tumor tracking using fast-kV switching dual-energy fluoroscopy on a benchtop system *Med. Phys.* **46** 3235–44
Hsieh S S and Pelc N J 2015 A dynamic attenuator improves spectral imaging with energy-discriminating, photon counting detectors *IEEE Trans. Med. Imaging* **34** 729–39
Hsieh S S and Pelc N J 2016 Improving pulse detection in multibin photon-counting detectors *J. Med. Imaging* **3** 023505
Hu Y, Xu S, Li B, Inscoe C R, Tyndall D A, Lee Y Z, Lu J and Zhou O 2024 Improving the accuracy of bone mineral density using a multisource CBCT *Sci. Rep.* **14** 3887
Huijben E M *et al* 2024 Generating synthetic computed tomography for radiotherapy: SynthRAD2023 challenge report *Med. Image Anal.* **97** 103276
IEC 61267:2005 2005 Medical diagnostic x-ray equipment - radiation conditions for use in the determination of characteristics (International Electrotechnical Commission) (available at: https://webstore.iec.ch/publication/5079)
International Commission on Radiation Units and Measurements 1993 ICRU Report 49: stopping powers and ranges for protons and alpha particles *No. 49 in ICRU Report* International Commission on Radiation Units and Measurements, Bethesda, MD
Kay S M 1993 *Fundamentals of Statistical Signal Processing: Estimation Theory* vol 1 (Prentice-Hall, Inc.)
Kurz C *et al* 2016 Investigating deformable image registration and scatter correction for CBCT-based dose calculation in adaptive IMPT *Med. Phys.* **43** 5635–46
Landry G *et al* 2015 Investigating CT to CBCT image registration for head and neck proton therapy as a tool for daily dose recalculation *Med. Phys.* **42** 1354–66
Landry G *et al* 2015 Phantom based evaluation of CT to CBCT image registration for proton therapy dose recalculation *Phys. Med. Biol.* **60** 595–613
Landry G and Hua C-h 2018 Current state and future applications of radiological image guidance for particle therapy *Med. Phys.* **45** 12744
Leibold D, Schaart D R and Goorden M C 2024 Optimizing proton stopping power ratio prediction with dual-energy cone-beam CT using the Cramér-Rao lower bound *Proc. SPIE* **12925** 129253N
Li B *et al* 2024 Low-cost dual-energy CBCT by spectral filtration of a dual focal spot x-ray source *Sci. Rep.* **14** 9886
Li B, Lee H C, Duan X, Shen C, Zhou L, Jia X and Yang M 2017 Comprehensive analysis of proton range uncertainties related to stopping-power-ratio estimation using dual-energy CT imaging *Phys. Med. Biol.* **62** 7056–74
Marsh J F, VanMeter P D, Rajendran K, Leng S and McCollough C H 2023 Ex vivo coronary calcium volume quantification using a high-spatial-resolution clinical photon-counting-detector computed tomography *J. Med. Imaging* **10** 043501

McCollough C H, Rajendran K, Leng S, Yu L, Fletcher J G, Stierstorfer K and Flohr T G 2023 The technical development of photon-counting detector CT *Eur. Radiol.* **33** 5321–30
Möhler C, Russ T, Wohlfahrt P, Elter A, Runz A, Richter C and Greilich S 2018 Experimental verification of stopping-power prediction from single- and dual-energy computed tomography in biological tissues *Phys. Med. Biol.* **63** 025001
Moskvin V P *et al* 2022 Accuracy of stopping power ratio calculation and experimental validation of proton range with dual-layer computed tomography *Acta Oncol.* **61** 864–8
Newhauser W D and Zhang R 2015 The physics of proton therapy *Phys. Med. Biol.* **60** R155–209
Ödén J, Zimmerman J, Bujila R, Nowik P and Poludniowski G 2015 Technical note: on the calculation of stopping-power ratio for stoichiometric calibration in proton therapy *Med. Phys.* **42** 5252–7
Peters N *et al* 2022 Reduction of clinical safety margins in proton therapy enabled by the clinical implementation of dual-energy CT for direct stopping-power prediction *Radiother. Oncol.* **166** 71–78
Peters N *et al* 2023 Consensus guide on CT-based prediction of stopping-power ratio using a Hounsfield look-up table for proton therapy *Radiother. Oncol.* **184** 109675
Poludniowski G, Landry G, DeBlois F, Evans P M and Verhaegen F 2009 SpekCalc: a program to calculate photon spectra from tungsten anode x-ray tubes *Phys. Med. Biol.* **54** N433–8
Rajendran K *et al* 2022 First clinical photon-counting detector CT system: technical evaluation *Radiology* **303** 130–8
Rigaud B, Simon A, Castelli J, Lafond C, Acosta O, Haigron P, Cazoulat G and de Crevoisier R 2019 Deformable image registration for radiation therapy: principle, methods, applications and evaluation *Acta Oncol.* **58** 1225–37
Roessl E and Herrmann C 2009 Cramér–Rao lower bound of basis image noise in multiple-energy x-ray imaging *Phys. Med. Biol.* **54** 1307–18
Saito M 2012 Potential of dual-energy subtraction for converting CT numbers to electron density based on a single linear relationship: conversion of energy-subtracted CT number to electron density *Med. Phys.* **39** 2021–30
Sandvold O F *et al* 2024 Hybrid spectral CT system with clinical rapid kVp-switching x-ray tube and dual-layer detector for improved iodine quantification *Proc. SPIE* **12925** 129251K
Sarrut D *et al* 2014 A review of the use and potential of the GATE Monte Carlo simulation code for radiation therapy and dosimetry applications: GATE for dosimetry *Med. Phys.* **41** 064301
Schneider U, Pedroni E and Lomax A 1996 The calibration of CT Hounsfield units for radiotherapy treatment planning *Phys. Med. Biol.* **41** 111–24
Seco J and Spadea M F 2015 Imaging in particle therapy: state of the art and future perspective *Acta Oncol.* **54** 1254–8
Seltzer S M and Berger M J 1982 Evaluation of the collision stopping power of elements and compounds for electrons and positrons *Int. J. Appl. Radiat. Isot.* **33** 1189–218
Siewerdsen J H, Daly M J, Bakhtiar B, Moseley D J, Richard S, Keller H and Jaffray D A 2005 A simple, direct method for x-ray scatter estimation and correction in digital radiography and cone-beam CT: x-ray scatter correction *Med. Phys.* **33** 187–97
Spronk D, Luo Y, Inscoe C R, Lee Y Z, Lu J and Zhou O 2021 Evaluation of carbon nanotube x-ray source array for stationary head computed tomography *Med. Phys.* **48** 1089–99
Stierstorfer K 2018 Modeling the frequency-dependent detective quantum efficiency of photon-counting x-ray detectors *Med. Phys.* **45** 156–66
Taasti V T *et al* 2017 Validation of proton stopping power ratio estimation based on dual energy CT using fresh tissue samples *Phys. Med. Biol.* **63** 015012
Taasti V T, Muren L P, Jensen K, Petersen J B B, Thygesen J, Tietze A, Grau C and Hansen D C 2018 Comparison of single and dual energy CT for stopping power determination in proton therapy of head and neck cancer *Phys. Imaging Radiat. Oncol.* **6** 14–19
Taasti V T, Petersen J B B, Muren L P, Thygesen J and Hansen D C 2016 A robust empirical parametrization of proton stopping power using dual energy CT *Med. Phys.* **43** 5547–60
Taguchi K 2021 Assessment of multienergy interpixel coincidence counters (MEICC) for charge sharing correction or compensation for photon counting detectors with boxcar signals *IEEE Trans. Radiat. Plasma Med. Sci.* **5** 465–75
Taguchi K, Schaart D R, Goorden M C and Hsieh S S 2025 Imaging performance of a $LaBr^3$: Ce scintillation detector for photon counting x-ray computed tomography: simulation study *Med. Phys.* **52** 158–70
Taguchi K, Stierstorfer K, Polster C, Lee O and Kappler S 2018 Spatio-energetic cross-talk in photon counting detectors: numerical detector model (PcTK) and workflow for CT image quality assessment *Med. Phys.* **45** 1985–98
Tanaka R *et al* 2010 Investigation on effect of image lag in fluoroscopic images obtained with a dynamic flat-panel detector (FPD) on accuracy of target tracking in radiotherapy *J. Radiat. Res.* **51** 723–31
Thummerer A *et al* 2020 Comparison of CBCT based synthetic CT methods suitable for proton dose calculations in adaptive proton therapy *Phys. Med. Biol.* **65** 095002
Van Der Sar S J, Brunner S E and Schaart D R 2021 Silicon photomultiplier-based scintillation detectors for photon-counting CT: a feasibility study *Med. Phys.* **48** 6324–38
Van Der Sar S J and Schaart D R 2025 Performance of x-ray photon-counting scintillation detectors under pile-up conditions at 60 keV *IEEE Trans. Radiat. Plasma Med. Sci.* 1–1
Wang A S, Harrison D, Lobastov V and Tkaczyk J E 2011 Pulse pileup statistics for energy discriminating photon counting x-ray detectors: pulse pileup statistics for photon counting detectors *Med. Phys.* **38** 4265–75
Wang A S and Pelc N J 2011 Sufficient statistics as a generalization of binning in spectral x-ray imaging *IEEE Trans. Med. Imaging* **30** 84–93
Wohlfahrt P, Möhler C, Richter C and Greilich S 2018 Evaluation of stopping-power prediction by dual- and single-energy computed tomography in an anthropomorphic ground-truth phantom *Int. J. Radiat. Oncol. Biol. Phys.* **100** 244–53
Xie Y, Ainsley C, Yin L, Zou W, McDonough J, Solberg T D, Lin A and Teo B-K K 2018 Ex Vivo validation of a stoichiometric dual energy CT proton stopping power ratio calibration *Phys. Med. Biol.* **63** 055016
Xu S, Hu Y, Li B, Inscoe C R, Tyndall D A, Lee Y Z, Lu J and Zhou O 2023 Volumetric computed tomography with carbon nanotube x-ray source array for improved image quality and accuracy *Commun. Eng.* **2** 71
Xu S, Li B, Inscoe C R, Bastawros D, Tyndall D A, Lee Y Z, Lu J and Zhou O 2023 Evaluation of the feasibility of a multisource CBCT for maxillofacial imaging *Phys. Med. Biol.* **68** 175012
Yang M, Virshup G, Clayton J, Zhu X R, Mohan R and Dong L 2010 Theoretical variance analysis of single- and dual-energy computed tomography methods for calculating proton stopping power ratios of biological tissues *Phys. Med. Biol.* **55** 1343–62